Surface analysis of N-doped TiO$_2$ nanorods and their enhanced photocatalytic oxidation activity

Yun Jeong Hwang [a], Sena Yang [b], Hangil Lee [c],*

[a] Clean Energy Research Center, Korea Institute of Science and Technology, Seoul 136-791, Republic of Korea
[b] Molecular-Level Interface Research Center, Department of Chemistry, KAIST, 305-701, Republic of Korea
[c] Department of Chemistry, Sookmyung Women's University, Seoul 140-742, Republic of Korea

ABSTRACT

We investigated the presence of Ti^{3+} defect sites on the surfaces of N-doped TiO$_2$ nanorods by using scanning transmission X-ray microscopy (STXM) and high-resolution photoemission spectroscopy (HRPES). The photo-oxidation activities of different types of N-doped TiO$_2$ nanorods were compared with each other and with their undoped nanorods. These nanorods were used to photocatalyze the oxidation of thiol molecules (i.e. 2-mercaptoethanol, benzenethiol, and 2-aminothiophenol) to disulfide and sulfonic ($-SO_3H$) species, and the conversion of CO to CO$_2$, and their photocatalytic activities towards these reactions were assessed using HRPES and a residual gas analyzer, respectively. Conversion to further oxidized sulfonic species was only achieved on the N-doped TiO$_2$ surface compared to the non-doped TiO$_2$ nanorods. In addition, we found that longer N-doped TiO$_2$ nanorods (NTR-150) showed higher photo-oxidation activity than NTR-60, which resulted from their increased number of defect sites and narrowed band-gap.

© 2016 Elsevier B.V. All rights reserved.

1. Introduction

TiO$_2$ has been intensively studied during the past several decades for energy and environmental applications such as photocatalysis, photoelectrodes in photovoltaic cells, photochromics, and sensing [1–5]. Although various semiconductors have been developed to utilize sunlight as an energy source, TiO$_2$ in particular remains one of the most widely used photocatalytic materials due to its high oxidizing power, high photostability, abundance, non-toxicity, and developed synthesis techniques [6,7]. During photocatalytic reactions, light is absorbed by TiO$_2$, and the excited electrons and holes participate in catalytic reactions on its surface. Therefore, developing an efficient TiO$_2$ photocatalyst requires improving both the light-absorption capability and catalytic activity of the TiO$_2$ surface.

The band gaps of currently available forms of TiO$_2$ are relatively wide (E$_g$ = 3.0–3.2 eV), and this width allows it to absorb only UV light, and leaves it inactive for the visible region. Therefore, figuring out how to narrow its band gap has been an important topic of research aiming to broaden its utility under ambient sunlight. The optical properties of semiconductors are determined by their electronic structure, which is strongly influenced by the dimensions or size of the material, the arrangement in the crystal structure, surface or defect structures, and chemical compositions [8]. For this reason, impurity doping has been widely performed to decrease the bandgap since the impurity element in TiO$_2$ can introduce electronic states in mid-gap regions or modify band edge states, leading to photoexcitation under visible light. For example, transition metals have been widely used to substitute the Ti^{4+} cation since they typically affect the conduction band states. Meanwhile, non-metals such as C and N can replace the O^{2-} anion [9–13], but relatively few studies have been done in this regard because differences in the charge states and ionic radii between the non-metal and the O^{2-} anion interrupt effective doping in TiO$_2$ [14].

Recent reports have indicated that N is effective in narrowing the band gap of TiO$_2$ because the 2p orbital of N can mix with 2p orbital of the O of TiO$_2$ and affect the valence band edge of the semiconductor [15]. The valence band states are important for photocatalytic oxidation reactions because the excited holes in the valence band are used for the oxidation reaction. Therefore, N-doping can strongly influence the catalytic activity as well as the visible light absorption capability [16,17]. However, whether the net effect of N-doping on the photocatalytic activity is positive or negative remains controversial because doping can introduce defects or surface states that can act as recombination centers or affect the catalytic activity. In addition, the performance of the

* Corresponding author.
E-mail addresses: easyscan@sookmyung.ac.kr, easyscan@gmail.com (H. Lee).

N-doped TiO$_2$ depends on the synthesis method. Therefore, more studies are required to understand the general behavior of N-doped TiO$_2$.

For carrying out such studies, nano-sized structures are more adaptable than the corresponding bulk materials, because their high surface-to-volume ratio yields a high tolerance for structural distortions. Their large surface area is also an advantage for photocatalytic applications and the newly exposed surface would be expected to display better catalytic activity than that displayed by the surface of the bulk material because chemical reactions occur on the TiO$_2$ surface. One-dimensional (1D) nanorod arrays in particular have been studied extensively, especially for photoelectrochemical cells [18–21] because of the advantage of facile charge separation along the 1D structure and short diffusion length across its diameter.

For this purpose, we here focused on N-doped TiO$_2$ nanorod arrays and their application as photocatalysts to study their active sites. Various spectroscopic surface analyses were used to characterize the electronic state of the N-doped TiO$_2$ nanorod which showed narrowing of the band gap and changes in the catalytic activity of photo-oxidation. Our previous study on the pristine TiO$_2$ nanorods prepared by hydrothermal method showed different level of nanorod length and defect state as a function of growth time [22], and it is expected that N-doping tendency and consequential photoactivity can be affected by the length of TiO$_2$ nanorods. Two different-length TiO$_2$ nanorods, denoted as NTR-60 and NTR-150, were synthesized and doped with nitrogen by carrying out annealing under an ammonia environment. Both types of N-doped TiO$_2$ nanorod samples were used to catalyze the oxidation of organic molecules under irradiation, and we found that the catalytic activity was enhanced with the longer N-doped TiO$_2$ nanorod arrays caused by the increased number of defect sites. In addition, the conversion of CO to CO$_2$ showed a similarly enhanced activity. We also compared in detail the morphologies and electronic properties of NTR-60 and NTR-150 by using scanning electron microscope (SEM), Raman spectroscopy, and scanning transmission X-ray microscopy (STXM) and also assessed their catalytic capacities (photo-catalytic oxidation and CO to CO$_2$ conversion) by using high-resolution photoemission spectroscopy (HRPES) and residual gas analyzer (RGA).

2. Experimental section

2.1. Preparation of N-doped TiO$_2$ nanorods

TiO$_2$ nanorods were hydrothermally prepared on a fluorine-doped tin oxide (FTO)-coated glass substrate following the previously reported method, and two different TiO$_2$ samples denoted as TR-60 and TR-150 were prepared by using growth times of 60 and 150 min, respectively [13]. To produce the corresponding N-doped samples, denoted as NTR-60 and NTR-150, each of the two TiO$_2$ nanorod samples were thermally treated in a tube furnace at 500 °C for one hour and cooled down slowly to room temperature, all in the presence of a continuous flow of 50 sccm of NH$_3$ gas.

2.2. Chemicals

Mercaptoethanol (2-ME; HOCH$_2$CH$_2$SH, Sigma Aldrich 99% purity), benzenethiol (BE; C$_6$H$_5$SH, Sigma Aldrich 95% purity), 2-aminothiophenol (2-ATP; C$_4$H$_4$SHNH$_2$, Sigma Aldrich 99% purity), O$_2$ and CO gas were purified by turbo pumping to remove impurities prior to being dosed onto two distinct N-doped TiO$_2$ nanorod array samples (NTR-60 and NTR-150) grown on FTO.

2.3. Photocatalytic oxidation reactions

To carry out the photocatalytic oxidation reactions, each N-doped TiO$_2$ nanorod array sample (NTR-60 and NTR-150) was first placed inside a vacuum chamber. 2-ME, BE, and 2-ATP were then introduced onto the NTR samples, respectively, by use of a direct doser, controlled by means of a variable leak valve. The pressure of the chamber was 1×10^{-6} Torr during dosing, and the quantities of 2-ME, BE, and 2-ATP were varied by adjusting the dosing time over the range of 0–360 s to provide 0–360 L (Langmuir). During the co-exposure of the three molecules (2-ME, BE, and 2-ATP) and molecular oxygen, UV light (λ = 365 nm, VL-4.LC Tube 1×4–Watt, Vilber Loumat) was illuminated on the NTR surface through a quartz viewport. To determine how many molecules were oxidized during the photocatalytic oxidation reaction, S 2p core-level HRPES spectra were obtained using photon energies of 230 eV and the photocatalytic activities of the NTR samples were compared.

2.4. Characterizations

The morphologies of the samples were characterized by using a field-emission scanning electron microscope (FE-SEM, FEI Inspect F50) operating at an acceleration voltage of 10 kV. Raman spectra were obtained by using a spectrometer (Horiba, ARAMIS) with an Ar ion CW (514.5 nm) laser. STXM images and X-ray absorption spectroscopy (XAS) data were obtained at the Pohang Light Source (10A beam line) using the monochromatic soft X-rays of the synchrotron source. Image stacks were acquired at 395–435 eV (N K-edge), 452–480 eV (Ti L-edge), and 525–560 eV (O K-edge) to extract the three X-ray absorption spectra from the region of interest in our samples. HRPES experiments were performed at the 8A2 beamline of the Pohang Accelerator Laboratory (PAL), which was equipped with an electron analyzer (R2000, Gamma Data Scienta). The Ti 2p, O 1s, N 1s, and S 2p core-level spectra were obtained using photon energies of 510, 590, 480, and 230 eV to enhance the surface sensitivity. The binding energies of the core level spectra were determined with respect to the binding energies of the clean Au 4f core level for the same photon energy. Valence-band spectra were acquired at photon energies of 80 eV to measure the changes in the band gap. All spectra were recorded in the normal emission mode. Mass spectrometric analyses were carried out using a Hiden RC 301 (mass range ∼300 amu) system in ultra-high vacuum conditions, and that was operated in positive-ion mode to measure the amounts of CO, O$_2$, and CO$_2$.

3. Results and discussion

The morphologies of our N-doped nanorod samples (Fig. 1(a) and (c)) and the reported non-doped TiO$_2$ nanorods [22] were nearly identical, indicating that our nitrogen doping process did not disrupt the shape of the TiO$_2$. The N-doped sample hydrothermally grown for 60 min (NTR-60) was observed by SEM to consist of short (∼50 nm in length) and bright TiO$_2$ rods attached on the dark FTO substrate (Fig. 1(a)). On the other hand, when the growth time was increased to 150 min (NTR-150), the sample showed elongated structures, ∼900 nm in length and ∼95 nm in width (Fig. 1(c)). A similar dependence of nanorod morphology on hydrothermal reaction time was reported for the TiO$_2$ nanorod array on the FTO substrate [22].

The electronic structures of NTR-60 and NTR-150 were also found to differ, albeit relatively modestly, according to the Raman spectroscopic results (Fig. 1b and d). Both samples yielded Raman shifts at about 445 and 609 cm^{-1}, typical rutile TiO$_2$ peaks associated with E$_g$ and A$_{1g}$ modes [23], and at 700 cm^{-1}, resulting from
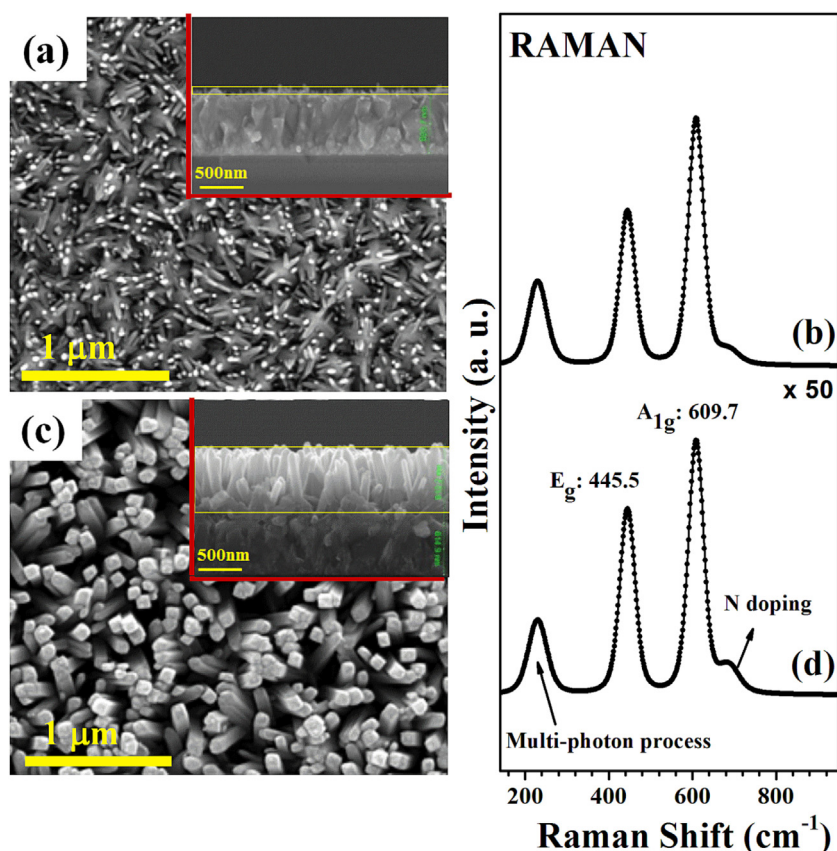
Fig. 1. (a,c) Top-view and cross-sectional SEM images, and (b,d) Raman spectra showing the electronic structures of N-doped TiO_2 nanorod arrays (NTR) grown on the FTO substrate for (a,b) 60 min (NTR-60) and (c,d) 150 min (NTR-150).
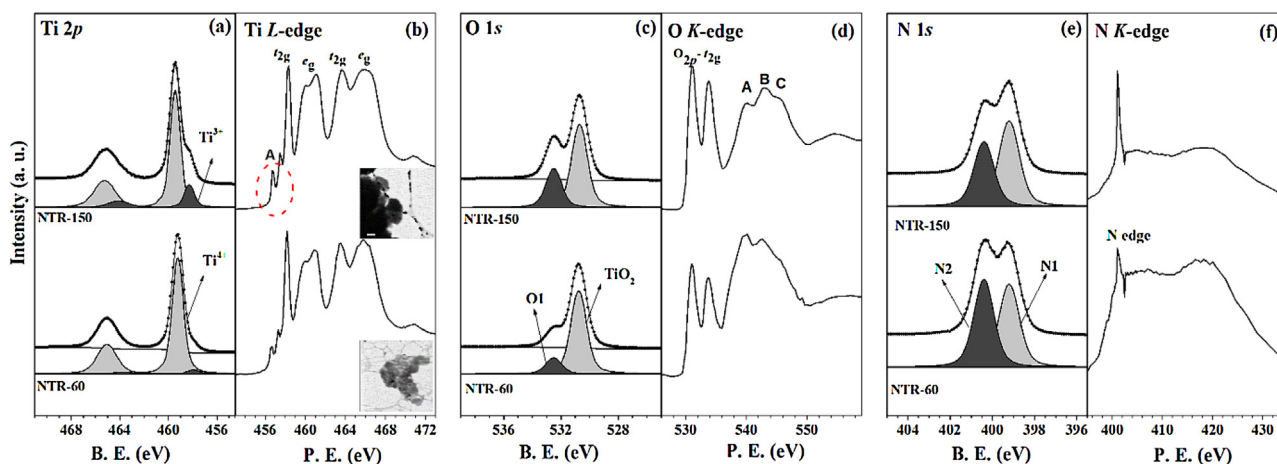

Fig. 2. (a) Ti 2p, (c) O 1s, and (e) N 1s core level HRPES spectra for NTR-60 and NTR-150. (b) STXM images ($4 \mu m \times 4 \mu m$) of the N-doped TiO_2 nanorod arrays and their corresponding (b) Ti $L_{2,3}$-edge, (d) O K-edge, and (f) N K-edge XAS spectra for NTR-60 (bottom) and NTR-150 (upper).

the nitrogen-induced defect [24]. The intensity of the latter peak, however, was a bit higher for NTR-150 than for NTR-60.

To further confirm the presence of N in NTR-60 and NTR-150 and to characterize the electronic states of their Ti, O, and N elements, HRPES spectra, STXM images and their corresponding XAS spectra were acquired (Figs. 2 and S1). Both the Ti 2p and O 1s core-level spectra contained two distinctive peaks: at 459.3 eV (Ti^{4+}) and 458.0 eV (Ti^{3+}) for Ti 2p, corresponding to Ti^{4+} and Ti^{3+}, respectively [25,26], and at 530.6 eV and 532.8 eV for O 1s, corresponding to O 1s in TiO_2 and O 1s related to the TiO_2 defect, respectively. These peaks clearly indicated the partial formation of Ti^{3+} defect structures in

the NTR samples. The major peaks were assigned to typical TiO_2 considering their binding energies at 459.3 ± 0.1 and 530.6 ± 0.1 eV and their peak shapes [27,28], and the minor ones were related to defect structures on the NTR surface. Previously, we observed that hydrothermally grown non-doped TiO_2 nanorod arrays also displayed a Ti^{3+} signal related to the defect structures, and the intensity of the defect peak increased as the nanorod growth time was increased from 60 min to 150 min. Based on the Ti 2p core-level spectra (see Fig. 2(a)), we calculated the ratio of the intensity of the Ti^{3+} (defect structure) peak to that of the Ti^{4+} (TiO_2) peak for NTR-60 as well as for NTR-150, and compared these ratios. In addi-
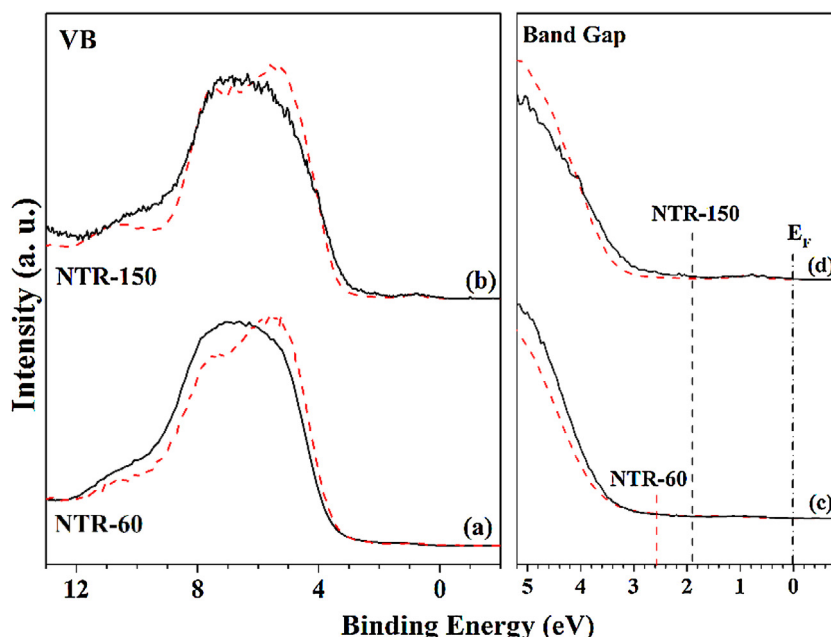
Fig. 3. (a,b) Valence spectra and (c,d) band gap measurements of (a,c) NTR-60 and (b,d) NTR-150. (Red dashed lines correspond to non-doped TR-60 and TR-150, as we determined previously [Ref. [13]). (For interpretation of the references to color in this figure legend, the reader is referred to the web version of this article.)

Table 1
Ratio of the intensities of the peaks corresponding to Ti^{3+} and Ti^{4+} of Ti $2p$ in the HRPES spectra and the intensity ratio of the A and t_{2g} peaks of the Ti L edge in the XAS spectra.

Intensity Ratio	TR-60	TR-150	NTR-60	NTR-150
Ti^{3+}/Ti^{4+}	0	0.12	0.04	0.21
A/t_{2g}	0.19	0.41	0.31	0.51

tion, we found more Ti^{3+} defects in the nanorod arrays for these N-doped samples (Table 1) than for the non-doped TR that we previously reported [22]. Moreover, in contrast to the case for NTR-60, which showed a small but measurable Ti^{3+} peak, no Ti^{3+} peak at all was obtained for (undoped) TR-60. These spectra showed that doping with nitrogen enhanced the (Ti^{3+}) defect structure. A greater number of defects in the NTR samples than in the TR samples was also indicated from comparing the intensities of the A (pre-edge) peak and t_{2g} peak from the Ti L-edge XAS. Both of the spectroscopic results showed a greater relative number of defect structures on the TiO_2 nanorod surface for long nanorods as well as N doped ones.

The Ti L-edge XAS spectra (Fig. 2(b)) of NTR-60 and NTR-150, in particular the ratio between the intensities of the $d_z{}^2$ and $d_x{}^2{}_{-y}{}^2$ peaks of the e_g orbital located near ∼460 eV, indicated that these samples mainly adopted the typical rutile crystal structure for TiO_2 [29,30]. But we also found different intensity ratios among the near edge peaks between NTR-60 and NTR-150. Compared to NTR-60, NTR-150 yielded two relatively large pre-edge peaks located at 456.7 and 457.4 eV (denoted as A), which were likely induced by the surface defect structure (Ti^{3+} state) [31]. The O K-edge XAS spectra showed the electronic transitions from the O $1s$ orbital to the O $2p$ orbital in the 530–540 eV region. The O $2p$ orbital was coupled with the split titanium $3d$ band of t_{2g} and e_g as shown in the Ti L-edge XAS [32], indicating the TiO_2 crystal structures.

The O K-edge shown in Fig. 2(d) displays the O $2p$-induced unoccupied density of states in the conduction band. That this spectrum derived from the rutile structure of TiO_2 was confirmed by the observed hybridization between O $2p$ and Ti $3d$ or Ti $4sp$, in particular 1) transitions into the O $2p$–Ti $3d$ hybridized bands, which split into two peaks due to the crystal field, and 2) transitions into O $2p$–Ti $4sp$ hybridized bands (peaks A, B, and C in Fig. 2(d)) [33]. In

detail, the first group was observed to consist of two major peaks in the 530–536 eV energy range, centered at approximately 531 and 534 eV. This group of peaks can be attributed to the transition of the O-$1s$ core-level 14 electrons to the hybridized O-$2p$ and Ti-$3d$ (t_{2g} and e_g) molecular orbitals [34] with a detailed structure sensitive to the local symmetry and ligand. The second group of peaks was observed to reside in the higher-energy region (537–550 eV) and to be associated with the O-$1s$ core-level transitions to the hybridized orbitals of the O-$2p$ and Ti-$4sp$ states; this group of transitions is quite sensitive to the level of long-range crystallographic order. The O-t_{2g} and O-e_g peaks became sharper and more separated (see NTR-150 in Fig. 2(d)), confirming the formation of the rutile structure. The spectra collected from the NTR-150 and NTR-60 samples were found to be very similar.

N $1s$ core-level spectra (Fig. 2(e)) and N K-edge XAS spectra (Fig. 2(f)) clearly confirmed the presence of the nitrogen element in our NTR-60 and NTR-150 samples, and N/Ti atomic ratio was more than three times in NTR-150 (N/Ti = 0.12) compared to NTR-60 (N/Ti = 0.035) as discussed in Fig. S2 and Table S1. Interestingly, the HRPES N $1s$ spectra showed two distinct N bonding features, marked as N1 at 398.2 eV and marked as N2 at 400.6 eV, and a relatively enhanced portion of the N1 peak over N2 was observed in NTR-150 compared to NTR-60 (Fig. 2(e)). According to the previous studies, generally, N1 peak could be the result of substituted nitrogen atoms which forms Ti-N (or N—Ti—O) bonds [35], and N2 peak is attributed to nitrogen to bond oxygen from interstitial N-atoms to O sites (N—O—Ti) [36]. Both the HRPES and XAS spectra showed differences in the Ti, O, and N electronic states between NTR-60 and NTR-150, and the N-doped TiO_2 nanorods showed more defects than did non-doped ones, despite their similar morphologies. Hence, we also suggest more defect structures and nitrogen doping on the surfaces of the TiO_2 NTR-150 nanorods than on the surfaces of the NTR-60 nanorods.

3.1. Comparison of band-gap narrowing between NTR-60 and NTR-150

Following the confirmation of nitrogen doping by the surface analysis, we investigated band gap shifts by acquiring valence-band
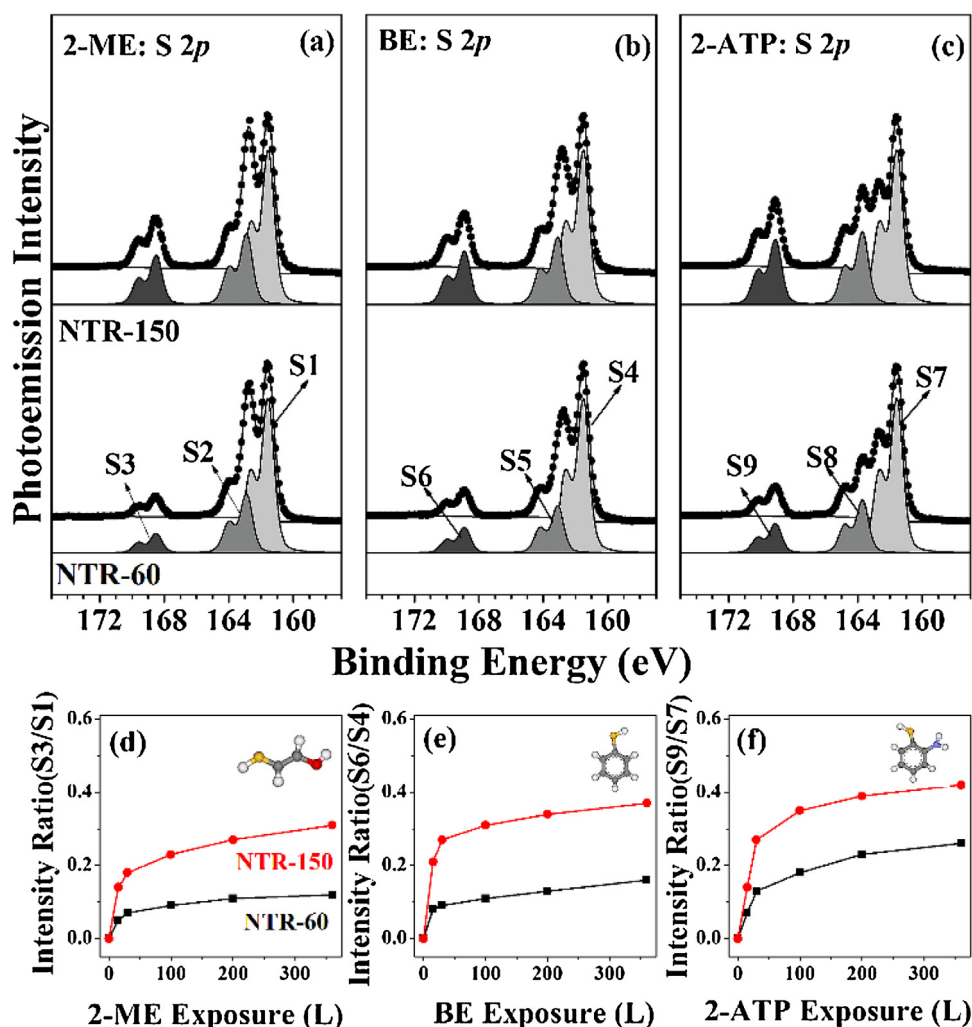
Fig. 4. HRPES S $2p$ core-level spectra of the NTR-60 and NTR-150 samples during photo-oxidation of (a) 2-ME (360 L), (b) BE (360 L), and (c) 2-ATP (360 L). The intensity ratios of (d) S3/S1, (e) S6/S4, and (f) S9/S7 showing the photocatalytic activity of the nanorods towards the 2-ME, BE, and 2-ATP oxidation reactions. (See text for definition of S1, S2, etc.) The inset shows the molecular structures of the compounds subjected to oxidation, and the yellow, red, gray, blue, and white balls indicate sulfur (S), oxygen (O), carbon (C), nitrogen (N), and hydrogen (H), respectively. (For interpretation of the references to color in this figure legend, the reader is referred to the web version of this article.)

Table 2
Ratios of oxidized sulfur signal intensities to unbound sulfur signal intensities, all resulting from exposure to 356-nm-wavelength UV light, as a function of the extent of exposure to the tested molecules.

Intensity ratio under 356-nm-wavelength UV light exposure						
Exposure (L)	2-ME (S3/S1)		BE (S6/S4)		2-ATP (S9/S7)	
	NTR-60	NTR-150	NTR-60	NTR-150	NTR-60	NTR-150
15	0.05	0.14	0.08	0.21	0.07	0.14
30	0.07	0.18	0.09	0.27	0.13	0.27
100	0.09	0.23	0.11	0.31	0.18	0.35
200	0.11	0.27	0.13	0.34	0.23	0.39
360	0.12	0.31	0.16	0.37	0.26	0.42

spectra. The pristine rutile TiO$_2$ has been reported to have a band gap of ∼3.0 eV [37,38]. The spectra of NTR-60 and NTR-150 (black lines of Fig. 3(a) and (b)) were observed to be very similar to that of pristine rutile TiO$_2$. Moreover, compared to the NTR peak, the TR peak (red dashed spectra) was located at a lower energy level, at 5 eV, indicating N-doping affects the electronic structure of TiO$_2$. As shown in the valence-band spectra of NTR in the right panel of Fig. 3, the band gap of NTR decreased from 3.0 eV to 2.6 eV for NTR-60 and to 1.94 eV for NTR-150 which were even smaller bandgap of TR-60 (E_g = 2.86 eV) and TR-150 (E_g = 2.15 eV). The narrower band

gap of NTR-150 may have resulted from its greater number of defect structures and higher amount of N-doping than found for NTR-60. As a result, we conclude that both N-doping and defect structures contribute to decrease the band gap in NTR.

3.2. Photocatalytic oxidation activity

Next, we determined the photocatalytic activities of each of the N-doped TiO$_2$ nanorods towards the oxidation of three different molecules, namely 2-ME, BE, and 2-ATP, each of which has a thiol
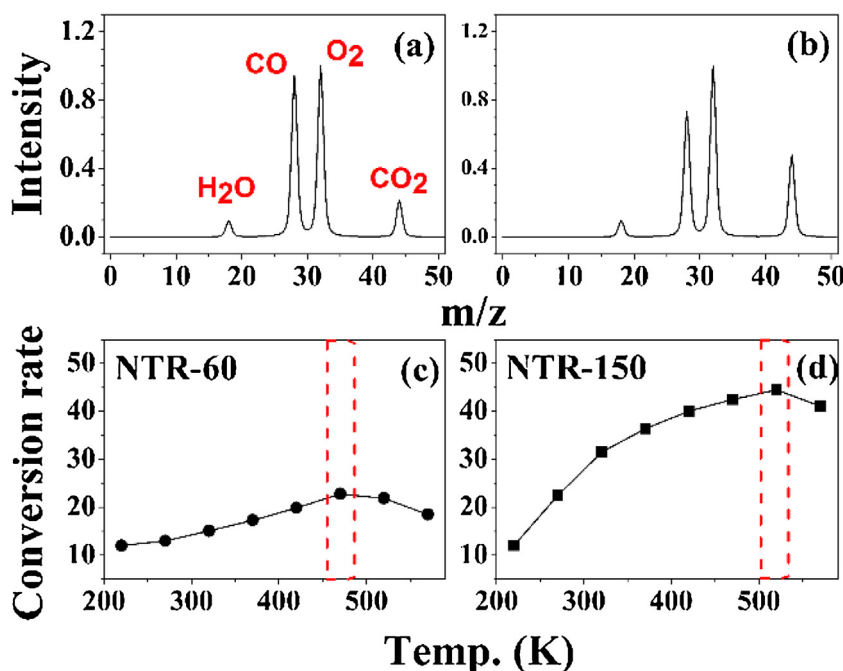
Fig. 5. Mass spectra of the result of the CO conversion reaction at 300 K with (a) NTR-60 and (b) NTR-150, and the rate of conversion from CO to CO_2 gas obtained with (c) NTR-60 and (d) NTR-150 as a function of reaction temperature.

(—SH) functional group. To measure the amount of the oxidation, the surface-sensitive S 2p core-level spectra were recorded using HRPES after exposure of the nanorods to 360 L of each molecule along with the same amount of oxygen under 365-nm-wavelength UV light illumination. As shown in Fig. 4(a)–(c), each case yielded an S 2p core-level spectrum having three distinct $2p_{3/2}$ peaks, at 161.5, 162.9, and 168.6 eV, which corresponded to the unreacted C—SH state (denoted as S1, S4, and S7 for 2-ME, BE, and 2-ATP, respectively), disulfide state (denoted as S2, S5, and S8), and sulfonic acid (SO$_3$H) state (denoted as S3, S6, S9) of the adsorbate on the TiO$_2$ nanorod surfaces, respectively [39,40].

Here, the unreacted states corresponded to unreacted thiol, while disulfide and sulfonic acid species were formed as a result of the oxidation of the thiol (—SH) group of these molecules. The sulfonic acid species is the more oxidized sulfur state with higher binding energy. Note that both NTR samples, i.e., NTR-60 and NTR-150, catalyzed the production of both types of oxidized sulfur states, while our previous (undoped) TR-150 sample yielded only the disulfide state [22]. Moreover, undoped TR-60 did not show any photo-oxidation activity towards 2-ME and 2-ATP. The HRPES measurements showed that doping the TiO$_2$ nanorods with N improved their photo-oxidation activities and yielded new oxidation products of the thiol molecules, implying that N-doping can affect the mechanistic pathway. The improved photocatalytic activity of the N-doped TiO$_2$ nanorods relative to the undoped nanorods can be explained by their increased number of defect sites and/or their having a smaller band gap.

Next, we calculated the ratio of the intensity of the unbound state peak at 161. 5 eV to that of the oxidized state (sulfonic acid state) peak at 168.6 eV for NTR-60 as well as for NTR-150, and compared these ratios in order to compare the oxidation activities of these two NTR surfaces (Fig. 4(d)–(f)). Table 2 summarizes the variations in the ratios of the sulfur peak signal intensities to compare the oxidation capacities as functions of exposure to 2-ME, BE, and 2-ATP under 365-nm-wavelength UV light, respectively. For each of these thiol-containing substrates, NTR-150 yielded a higher ratio of the oxidized sulfur state to the thiol state than did NTR-60. Specifically, NTR-150 catalyzed a 2.5 times higher photo-oxidative

conversion of the thiol group in the 2ME and BE molecules than did NTR-60 based on the intensity ratios S3/S1 and S6/S4. Also, the intensity ratio S9/S7 showed that oxidation of 2-ATP was 1.8 times higher with NTR-150 than with NTR-60.

3.3. CO conversion

Since the oxidation of CO to CO_2 is used as a standard for comparing the activities of photocatalysts of oxidation reactions, we also carried out this reaction in the presence of NTR-60 and NTR-150, respectively. These CO to CO_2 conversions were carried out under UV irradiation and at various temperatures (200 K–700 K), and were assessed by using mass spectroscopy. Fig. 5(a) and (b) shows the typical mass spectra obtained after CO oxidation at 300 K for each NTR. As shown in Fig. 5c and d, NTR-150 clearly yielded a faster conversion of CO to CO_2 than did NTR-60 for nearly all reaction temperatures tested. For example, at 500 K, the conversion rate when using NTR-150 was almost double that when using NTR-60. The more numerous defect sites on the NTR-150 surface thus may have contributed to its enhanced oxidation activity for the CO oxidation reaction as well as for the thiol oxidation reaction described above. Also as seen in Fig. 5c and d, for each NTR but especially for NTR-150, the conversion rate increased with temperature for most of the temperature range tested. Note, however, that as calculated for these figures, the CO to CO_2 conversion rate gave the appearance of decreasing when the reaction temperature was raised above 550 K. But this result occurred because, at such high temperatures, the adsorbed molecules (CO and O_2) decompose, with this decomposition reaction occurring together with the CO to CO_2 conversion reaction and even becoming dominant.

4. Conclusions

N was doped in hydrothermally grown TiO$_2$ nanorod arrays by carrying out a thermal treatment under ammonia flow, and N doping was confirmed by HRPES. Compared to undoped TiO$_2$ nanorods, the N-doped TiO$_2$ nanorod arrays showed enhanced photocatalytic activity for oxidation of thiol molecules to the sulfonic acid species,

which was not observed for the undoped TiO_2 nanorods. In addition, more oxygen vacancies and Ti^{3+} defect states were observed for the long N-doped nanorods (NTR-150) than for the short ones (NTR-60) as indicated by surface spectroscopic techniques such as Raman, HRPES, and XAS. Higher oxidation activities of NTR-150 were confirmed by various reactions such as oxidations of three different thiol molecules (2-ME, BE, 2-ATP), and conversion of CO to CO_2. A greater number of surface defect states on the N-doped TiO_2 nanorod array apparently contributed to its improved catalytic activity.

Acknowledgements

Appendix A. Supplementary data

Supplementary data associated with this article can be found, in the online version, at http://dx.doi.org/10.1016/j.apcatb.2016.11.038.

References

[1] C.L. Pang, R. Lindsay, G. Thornton, Chem. Soc. Rev. 37 (2008) 2328.
[2] Y. Ma, X. Wang, Y. Jia, X. Chen, H. Han, C. Li, Chem. Rev. 114 (2014) 9987.
[3] A.J. Nozik, J. Miller, Chem. Rev. 110 (2010) 6443.
[4] A.J. Frank, N. Kopidakis, J. van de Lagemaat, Coord. Chem. Rev. 248 (2004) 1165–1179.
[5] Y. Ohko, T. Tatsuma, T. Fujii, K. Naoi, C. Niwa, Y. Kubota, A. Fujishima, Nat. Mater. 2 (2003) 29–31.
[6] M. Ni, M.K.H. Leung, D.Y.C. Leung, K. Sumathy, Renew. Sustain. Energy Rev. 11 (2007) 401–425.
[7] A.L. Linsebigler, G. Lu, J.T. Yates, Chem. Rev. 95 (1995) 735–758.
[8] T. Umebayashi, T. Yamaki, H. Itoh, K. Asai, J. Phys. Chem Solids 63 (2002) 1909–1920.
[9] P. Mazierski, M. Nischk, M. Golkowska, W. Lisowski, M. Gazda, M.J. Winiarski, T. Klimczuk, A. Zaleska-Medynska, Appl. Catal. B: Environ. 196 (2016) 77–88.
[10] N. Lu, X. Quan, J. Li, S. Chen, H. Yu, G. Chen, J. Phys. Chem. C 111 (2007) 11836–11842.
[11] Q. Xiang, J. Yu, W. Wang, M. Jaroniec, Chem. Commun. 47 (2011) 6906–6908.
[12] Y. Shao, C. Cao, S. Chen, M. He, J. Fan, J. Chen, X. Li, D. Li, Appl. Catal. B: Environ. 179 (2015) 344–351.
[13] T. Ohno, T. Mitsui, M. Matsumura, Chem. Lett. 32 (2003) 364–365.
[14] X. Chen, S.S. Mao, Chem. Rev. 107 (2007) 2891–2959.
[15] C. Di Valentin, E. Finazzi, G. Pacchioni, A. Selloni, S. Livraghi, M.C. Paganini, E. Giamello, Chem. Phys. 339 (2007) 44–56.
[16] S. Yang, Y. Kim, E. Jeon, J. Baik, N. Kim, H. Kim, H. Lee, Catal. Commun. 81 (2016) 45–49.
[17] N. Aman, N.N. Das, T. Mishra, J. Environ. Chem. Eng. 4 (2016) 191–196.
[18] S.U.M. Khan, M. Al-Shahry, W.B. Ingler Jr., Science 297 (2002) 2243–2245.
[19] J.H. Bang, P.V. Kamat, Adv. Funct. Mater. 20 (2010) 1970–1976.
[20] A. Wolcott, W.A. Smith, T.R. Kuykendall, Y. Zhao, J.Z. Zhang, Small 5 (2009) 104–111.
[21] I.S. Cho, Z. Chen, A.J. Forman, D.R. Kim, P.M. Rao, T.F. Jaramillo, X. Zheng, Nano Lett. 11 (2011) 4978–4984.
[22] Y. Hwang, S. Yang, E. Jeon, H. Lee, Appl. Catal. B: Environ. 10 (2016) 480–486.
[23] G. Yang, Z. Jiang, H. Shi, T. Xiao, Z. Yan, J. Mater. Chem. 20 (2010) 5301–5309.
[24] J. Surmacki, P. Wroński, M. Szadkowska-Nicze, H. Abramczy, Chem. Phys. Lett. 566 (2013) 54–59.
[25] U. Diebold, T.E. Madey, Surf. Sci. Spectra 4 (1996) 227.
[26] H. Lee, M. Shin, M. Lee, Y. Hwang, Appl. Catal. B: Environ. 165 (2015) 20–26.
[27] J.F. Moulder, W.F. Stickle, P.E. Sobol, K.D. Bomben, Handbook of X-ray Photoelectron Spectroscopy, Physical Electronics, Inc., Eden Prairie, MN, 1995.
[28] W.E. Kaden, T. Wu, W.A. Kunkel, S.L. Anderson, Science 326 (2009) 826–830.
[29] L.D. Finkelstein, E.I. Zabolotzky, M.A. Korotin, S.N. Shamin, S.M. Butorin, E.Z. Kurmaev, J. Nordgren, X-ray Spectrosc. 31 (2002) 414.
[30] P. Krüger, Phys. Rev. B 81 (2010) 125121.
[31] S.B. Singh, Y. Wang, Y. Shao, H. Lai, S. Hsieh, M.V. Limaye, C. Chuang, H. Hsueh, H. Wang, J. Chiou, H. Tsai, C. Pao, C. Chen, H. Lin, J. Lee, C. Wu, J. Wu, W. Pong, T. Ohigashi, N. Kosugi, J. Wang, J. Zhou, T. Regier, T. Sham, Nanoscale 6 (2014) 9166.
[32] Y. Hwu, Y.D. Yao, N.F. Cheng, C.Y. Tung, H.M. Lin, Nanostruct. Mater. 9 (1997) 355.
[33] S.J. Stewart, M. Fernandez-Garcia, C. Belver, B.S. Mun, F.G. Requejo, J. Phys. Chem. B 110 (2006) 16482.
[34] L. Soriano, M. Abbate, J. Vogel, J.C. Fuggle, A. Fernandez, A.R. Gonzalezelipe, M. Sacchi, J.M. Sanz, Surf. Sci. 290 (1993) 427.
[35] B. Viswanathan, K.R. Krishanmurthy, Int. J. Photoenergy 269654 (2012) 1–10.
[36] C. Bittencourt, M. Rutar, P. Umek, A. Mrzel, K. Vozel, D. Arcon, K. Henzler, P. Kruger, P. Guttmann, RSC Adv. 5 (2015) 23350–23356.
[37] C. Burda, Y. Lou, X. Chen, A.C.S. Samia, J. Stout, J.L. Gole, Nano Lett. 3 (8) (2003) 1049–1051.
[38] G.I.N. Waterhouse, A.K. Wahab, M. Al-Oufi, V. Jovic, D.H. Anjum, D. Sun-Waterhouse, J. Llorca, H. Idriss, Sci. Rep. 3 (2013) 2849–2853.
[39] Y. Hwu, Y.D. Yao, N.F. Cheng, C.Y. Tung, H.M. Lin, Nanostruct. Mater. 9 (1997) 355.
[40] E. Jeon, S. Yang, Y. Kim, N. Kim, H. Shin, J. Baik, H. Kim, H. Lee, Nanoscale Res. Lett. 10 (361) (2015) 1–8.